Chemical Geology 269 (2010) 197–209

Contents lists available at ScienceDirect

Chemical Geology

journal homepage: www.elsevier.com/locate/chemgeo

Intense fracturing and fracture sealing induced by mineral growth in porous rocks

Catherine Noiriel [a], François Renard [b,c,*], Mai-Linh Doan [d], Jean-Pierre Gratier [d]

[a] Laboratoire Géosystèmes, Université de Lille I, CNRS, 59655 Villeneuve d'Ascq, France
[b] University Joseph Fourier, Grenoble I, CNRS, OSUG, Laboratoire de Géodynamique des Chaînes Alpines, BP 53, 38041 Grenoble, France
[c] Physics of Geological Processes, University of Oslo, Norway
[d] University Joseph Fourier, Grenoble I, CNRS, OSUG, Laboratoire de Géophysique Interne et Tectonophysique, BP 53, 38041 Grenoble, France

ARTICLE INFO

Article history:
Received 10 July 2009
Received in revised form 28 September 2009
Accepted 29 September 2009

Editor: J. Fein

Keywords:
Force of crystallization
Crystallization pressure
Fracture sealing
Salt
Fluid–rock interaction
Damage

ABSTRACT

Mineral precipitation in the pores of a rock may exert a force, which is called crystallization pressure. This process has been studied experimentally and results bring a new look on the way fractures may develop and seal in natural systems. Cylindrical core samples of porous limestone and sandstone were left for several weeks in contact with an aqueous solution saturated with sodium chloride, at 30 or 45 °C, under axial normal stress in the range 0.02–0.26 MPa. The fluid was allowed to rise in the core samples by capillary forces, up to a controlled height where evaporation and precipitation occurred. The uniaxial deformation of the samples was measured using high-resolution displacement sensors. The samples were characterized using computed X-ray tomography, allowing therefore imaging in 3D the intensity and localization of the damage. Two kinds of damage could be observed. Firstly, small rock fragments were peeled from the sample surface. Secondly, and more interestingly, fracture networks developed, by nucleation of microcracks at the interface where evaporation occurred, and propagation to the free surface. Two families of fractures could be identified. A first set of sealed fracture parallel to the evaporation front is directly induced by crystallization pressure. A second fracture network, perpendicular to the evaporation front, accommodates the first set of fractures. An analytical model where fluid flow is coupled to evaporation, vapour transport, and localization of mineral precipitation explains the shape of this fracture network.

1. Introduction

The growth of minerals in confined environments occurs in many places in the Earth's crust, from veins in the metamorphic domains to pore space in sedimentary rocks. It has been proposed that such crystallization, from a supersaturated fluid, can induce mechanical forces in the solid, which may even lead to permanent damage (for a review see Fletcher and Merino, 2001; Wiltschko and Morse, 2001; Rijniers et al. 2005).

This can also occur during hydration or oxidation reactions or mineral replacement (Putnis, 2002) where volume changes are involved. Several classes of growth process, in which chemical reactions may modify the state of stress and lead to permanent deformation are vein initiation and growth (Fletcher and Merino, 2001), hydration of metastable phases in cement (Steiger et al. 2008), spheroidal weathering and reaction-induced fracturing in mafic or ultramafic rocks (e.g. Chatterjee and Raymahashay, 1998; Royne et al., 2008), and septarian formation (Fletcher and Merino, 2001). This effect is also well-known when salts grow in porous rocks, such as building monuments, causing rock crumbling, weathering, and limiting the durability of the constructions (Wellman and Wilson, 1965; Scherer, 2004; Ruiz-Agudo et al. 2007; Angeli et al. 2008). Another case corresponds to salt damage close to injection wells in the context of CO_2 geological sequestration. When CO_2 is injected into a reservoir in a purpose of permanent geological storage, it can displace the salted pore fluids, dry them, and may induce massive salt precipitation around the borehole (Muller, et al., 2009).

When precipitating in confined pores, salt minerals induce a crystallization pressure that may potentially damage the reservoir. The extent of salt damage in porous rocks due to crystallization pressure appears to be largely a function of the solution supersaturation, the interfacial energy of the crystal–liquid interface, the localization of precipitation, the growth rate, and the mechanical response of the host rock. A condition for damage to occur is that a crystal continues to grow even in a confined space, thus exerting stress on the rock minerals. Experimental evidence that growing crystals can exert pressure has been provided for more than one hundred and fifty years (Lavalle, 1853; Taber, 1916). It was observed that a crystal placed in a container was pushed upward during growth by precipitation on its bottom surface. From experimental observations the authors concluded that a crystal continues to grow upon its load only if a solution film exists separating the loaded face from the container (Correns, 1949; Weyl, 1959). The solution film acts as a diffusion path allowing exchange of ions between the crystal and the solution. It originates from repulsive forces between the solution and

* Corresponding author.
E-mail address: francois.renard@ujf-grenoble.fr (F. Renard).

0009-2541/$ – see front matter © 2009 Elsevier B.V. All rights reserved.
doi:10.1016/j.chemgeo.2009.09.018

the crystal, i.e. interfacial tension differences at the salt–solution, the salt–rock, and the solution–rock interfaces. If one of its faces is in contact with a supersaturated solution, the crystal exerts a force, called force of crystallization. The degree of supersaturation required for growth to occur increases with increasing stress on the growth contact surface (Owen and Brinkley, 1941).

Crystallization pressure is then expected to generate damage into the sample. In order to study the effect of precipitation of minerals on the development of fracture networks and their various sealing processes, we have developed an experimental approach using sodium chloride. This salt is allowed to precipitate into stressed porous sandstone and limestone core samples. With this model system, the coupling between salt precipitation and core sample deformation has been measured. The damage patterns are imaged using 3D X-ray computed microtomography. Our experimental effort is done to better characterize this specific damage. We show that the precipitation damages the rock by the formation of microcracks that evolve into sealed fractures, and ultimately induce the development of secondary non-sealed fracture network.

In the following we first review the mechanisms of crystallization pressure. Then, we describe the experimental techniques. Finally, we analyze the damage patterns and propose a simplified analytical model that explains why rock samples may fracture or not, depending on the position of the evaporation front inside the core samples.

2. Crystallization pressure

Crystallization pressure is the result of a mechano-chemical interaction between minerals in the rock and the interstitial solution (Weyl, 1959). Three mechanisms of crystallization pressure may be identified. Firstly, local precipitation can be due to differences in mineralogy, crystal or pore size, and degree of crystal purity. If spatial difference in mineral solubility exists, diffusion in the solution due to concentration gradient will cause a gradual change by dissolution of the most soluble phase and crystallization of the supersaturated one. The second mechanism is similar to the pressure solution mechanism: mineral grains dissolve at contact points, where pressure is higher than in the solution, and precipitate around the grain contact. In this case, the material locally dissolved is precipitated so that not global change of chemical composition can take place. Finally, cementation or leaching of sediment can also occur by the transport of supersaturated pore fluids, when the system is open and fluid transport is driven by pressure or temperature gradients.

The removal or deposition of matter in the area of contact between grains implies that a solution film exists between minerals (Weyl, 1959). In the absence of such solution film, the growth of the crystal would stop and no stress could be generated since it would be impossible to add material along the contact zone. The presence of this film, which is necessary for the diffusion of solutes to the precipitation site, was assumed by Weyl (1959) and its thickness is of the order of several nanometers (Renard and Ortoleva, 1997; Dysthe et al. 2002).

2.1. Thermodynamic forces involved in the force of crystallization

Dissolution and crystallization under pressure result from mineral solubility variation and solution saturation changes, which involve energy changes in the crystal lattice or at the mineral surface. Consider a monomolecular solid which can react according to the reaction: $A \leftrightarrow A_{(aq)}$.The stress applied along a fluid–rock interface at constant temperature under a pressure P induces a variation of chemical potential of the stressed solid at the pressure P compared to a reference state pressure P_0:

$$\mu_{sT,P} = \mu_{sT,P_0} + \int_{P_0,V_{P0}}^{P,V_P} V_{s(P,T)}\,dP \tag{1}$$

$$\mu_{sT,P} = \mu_{sT,P_0} + V_s\Delta P + \Delta P\Delta V_s \tag{2}$$

where T is the temperature (K), and V_P and V_{P_0} are the volume at pressure P and P_0, respectively. Values of ΔV_s are very small at low pressure difference and can be neglected. Then, the variation of chemical potential can be expressed:

$$\mu_{sT,P} = \mu_{sT,P_0} + V_s\Delta P. \tag{3}$$

The chemical potential, μ_l, of a solute in equilibrium with the solid at pressure P_0 and P is given by, respectively:

$$\mu_{lT,P_0} = \mu^0_{lT,P_0} + RT\ln a_0, \tag{4}$$

and

$$\mu_{lT,P} = \mu^0_{lT,P_0} + RT\ln a \tag{5}$$

where R is the gas constant ($8.31\ \mathrm{MPa\,cm^3\,mol^{-1}\,K^{-1}}$), a_0 is the solute activity of the saturated solution at P_0, and a is the solute activity of the saturated solution at P. Considering the equilibria between the solid and the solution at the same pressure, the two chemical potentials are equal:

$$\mu_s = \mu_l. \tag{6}$$

Using Eqs. (3)–(5), it follows that:

$$\mu^0_{lT,P_0} + RT\ln a = \mu^0_{lT,P_0} + RT\ln a_0 + V_s\Delta P. \tag{7}$$

It follows from Eq. (7) that an increase of pressure leads to an increase of the solubility of the solid. Similarly, it is possible to derive the maximum stress ΔP that can be produced from the supersaturation of a solution:

$$\Delta P = \frac{RT}{V_s}\ln\frac{a}{a_0}. \tag{8}$$

This expression is close to the one proposed in the reference work of Correns and Steinborn (1939) and Correns (1949), since concentrations are assimilated to activities:

$$\Delta P = \frac{RT}{V_s}\ln\frac{C}{C_0} \tag{9}$$

where C is the concentration of the supersaturated solution and C_0 the equilibrium concentration of the solid in solution at standard pressure ($\mathrm{mol\,m^{-3}}$). However, assumption of equivalence between ion concentration and activity is valid only for dilute solutions, since the activity decreases as ionic strength increases. In addition, when salts are involved in the reaction instead of monomolecular crystals, one must consider the ionic activity product and the equilibrium constant of the reaction instead of C and C_0, respectively. This is discussed by Flatt et al. (2007).

If the solution is supersaturated, precipitation in the area of contact between the crystal and the pore wall will take place if the ratio of the supersaturation to stress coefficient of solubility is greater than the normal average stress between the crystal and the pore wall (Rodriguez-Navarro and Doehne, 1999). If the stress is increased above the limit, pressure enhanced dissolution will take place. Eq. (8) shows the analogy with pressure solution: if stress is applied at a contact point between two grains that are in equilibrium with a fluid, the fluid in contact will experience an undersaturation, resulting in material dissolution along the grains contact. However, if the fluid is supersaturated away from the contact, diffusion into the point contact leads to precipitation of material and increases in stress at the point contact. On the basis of this equation, several authors (Winkler and

Singer, 1972; Maliva and Siever, 1988; Fletcher and Merino, 2001; Steiger, 2005a) calculated the pressures exerted during precipitation of most common minerals (calcite, quartz, gypsum, and halite) and showed it could be high enough to disintegrate porous rocks.

To allow the development of a crystallization pressure, the crystal must be confined and grow against the confining stress on the rigid crystal wall. As long as a crystal has the possibility to grow freely within the pore, in drained conditions, the necessary confinement condition for crystallization pressure is not reached. The mode of accommodation (i.e. deformation) of that growth by the host rock regarding the rate of growth is also important (Fletcher and Merino, 2001). Two conditions may lead to confinement in the pore: the growth kinetics that varies for the different faces of the crystal, or the pore size distribution.

With pressure solution processes, the pore solution in equilibrium with the loaded surface of a crystal is supersaturated with respect to the unloaded faces (Fig. 1a). However, if the kinetics of growth on the unloaded surfaces is much faster than either the kinetics of dissolution on the loaded surface or the kinetics of mass transfer from loaded to unloaded surfaces, the supersaturation may be consumed by the growth process and the pressure cannot be maintained.

Crystallization pressure can also be the result of an equilibrium situation where the unloaded face of a growing crystal exhibits the same solubility increase as the loaded face due to the curvature of the different faces (Everett, 1961). This situation does occur, for example, in a spherical pore bordered with small cylindrical entrances (see Steiger, 2005b and Fig. 1b). In this case, growth of the crystal into the smallest pores requires higher saturation of the pore solution due to the large curvature. Due to their different size, the crystal in the pore is under enhanced pressure compared to the particle in the cylindrical small pore entrance. The crystallization pressure is given by surface energy difference (Everett, 1961; Steiger, 2005a):

$$\Delta P = 2\gamma_{cl}\left(\frac{1}{r_1}-\frac{1}{r_2}\right) \quad (10)$$

where γ_{cl} ($N m^{-1}$) is the interfacial tension between the solid and the liquid, r_1 refers to the radius of a smaller pore adjacent to a large pore of radius r_2 where crystal grows.

2.2. Origin of the supersaturation and damage

In order to reproduce fracturing processes associated with crystal growth in the lab, one must generate high supersaturation within times as short as possible. Some processes with very slow kinetics, as pressure solution, are not very well adapted for such studies under laboratory conditions, because they are too slow, even if they are very efficient in nature. Evaporation can be one of the driving forces for generating high supersaturation within relatively short periods of time (days–months). Rodriguez-Navarro and Doehne (1999) pointed out that important difference in salt damage level in building stones can be observed under varying relative humidity conditions: less damage is observed at higher relative humidity. Indeed, under low relative humidity conditions, evaporation rate of the saline solution is enhanced. High supersaturation is rapidly reached at the limits of the capillary fringe, where salt precipitation concentrates (Fig. 1c). Hence damage resulting from high crystallization pressure will be promoted there.

For halite, the supersaturation rarely reaches more than 10% weight (Chatterji, 2000). According to the calculation of Flatt (2002) for salt precipitation, the water activity decreases from 0.755 (saturation) to 0.72 (10% supersaturation). This would indicate that halite precipitation could produce a pressure in the range 20.5–41 MPa, depending on the geometry of the pore. The pore radius required for this pressure to develop under equilibrium would be 4 nm, using a value of the surface tension $\gamma_{cl} = 0.1\ J m^{-2}$. Such high pressures in porous rocks may reach the tensile strength of the material, promoting permanent damage.

The distribution of salt in the pores is controlled by several kinetic processes: supply of water, evaporation rate, diffusion of dissolved species away from the site of evaporation and nucleation and growth of the crystal (Scherer, 2006). For example, Rodriguez-Navarro and Doehne (1999) observed in their salt precipitation experiments two opposite cases. In the case of halite precipitation, the smallest pores (0.001–0.2 μm) were filled preferentially. Conversely, for sodium sulphate precipitation, experimental observations show mainly precipitation in pores in the range 0.8–1 μm diameter.

Sedimentary rocks have relatively low strength, because they contain flaws that can easily propagate into fractures. The tensile strength of many limestones and sandstones is comprised between 1 and 9 MPa. To reach the critical stress for fracture propagation, the crystal must propagate through the porous network over a distance large enough such that its stress field interacts with that of the fracture in question. It can be argued that the stress fields of isolated region of crystal must overlap and percolate in order to promote macroscopic crack growth. After the rupture, crystallization is concentrated in the fracture because evaporation is accelerated at the same time as the structure opens (Zehnder and Arnold, 1989).

3. Materials and method

3.1. Rock samples

Two porous rocks with different pore structure and mineralogical composition were used in the experiment. The Lavoux limestone, a Callovian age peloidal and bioclastic grainstone, was sampled in a quarry (Vienne, France). The rock is a quasi-pure limestone essentially

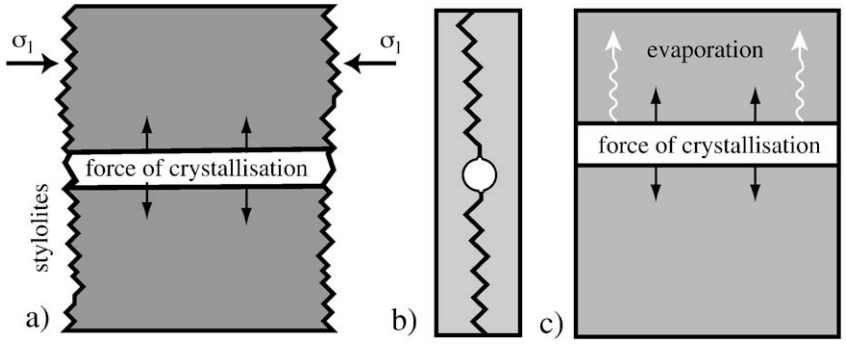

Fig. 1. Main principles of the force of crystallization. a) When dissolution occurs along surfaces perpendicular to the main compressive stress (stylolites), surpersaturation is induced along the path of diffusion that may enhance the opening of vein by the force of crystallization. b) In case of spherical pore bordered with small cylindrical entrances (adapted from Steiger 2005b), growth of the crystal into the smallest pores requires higher saturation of the pore solution due to the large curvature; c) Force of crystallization does also occur along a precipitation front into a porous medium, for example when evaporation can localize the precipitation along a well-developed interface, which may evolve into a fracture: it is the principle used in our experiment (Fig. 2).

composed of micritic peloids and echinoderm fragments cemented during secondary crystallization process. The mean porosity is 23%. Hg-porosity analysis shows that the pore distribution is trimodal. The porosity is mainly composed by pores of 0.1–0.7 µm in size, which correspond to intra-porosity of the micritic peloids. Two other families of pores of about 1 µm and 100 µm in size correspond to the inter-grain porosity. The larger corresponds to macroscopic porosity obtained by selective leaching of peloids during possible recent meteoric diagenesis.

The Adamswiller sandstone, a Bundsandstein age sandstone, was sampled in a quarry (Bas-Rhin, France). The rock is composed of quartz (71%), feldspar (9%) with little alteration, clay (11%), mica (5%), and iron and titan oxides. Its porosity if close to 23%, the mean grain size is 0.18 mm (David et al. 1994), and the average pore size is close to 90 µm. It is worth noting that the rock initially presents pressure dissolution patterns which result from diagenesis events.

3.2. Force of crystallization experiments

The specific apparatus designed for the capillary rise experiment is shown in Fig. 2. It consists of a stiff aluminium frame in which the sample is left under moderate stress, and on which several sensors could be attached. Eleven cylindrical samples of 23 mm diameter and between 60 and 130 mm long were cored from Lavoux limestone (LAV-1 to LAV-10) and Adamswiller sandstone (ADA-1) block samples. The half lower part of the cores was jacked with a rubber sleeve to prevent peripheral evaporation. As the capillary rise in the rock samples is expected to be largely higher than the maximum length that it is possible to drill within the block, a set of 125 mm long capillary tubes (Hirshmann ringcaps 10 and 25 µl) was placed under the sample in order to reduce the capillary pressure (Fig. 2). Then, the core samples were let in contact, through the set of capillary tubes, with a saturated sodium chloride solution prepared from reagent-grade NaCl dissolved in deionised water. The solution rose in the sample by capillarity until an equilibrium capillary fringe was reached. At this moment, water evaporated and induced supersaturation of the solution, which in turn induced halite precipitation. The height of the solution in the reservoir was kept constant during all the duration of the experiment (see Fig. 2).

During the experiment, the set-up was placed into an air oven at a constant temperature of 30 or 45 °C. Both temperature and relative humidity were monitored using a U12 data logger (Hobo©) at a frequency of three measurements per hour. It was verified that the relative humidity remained more or less constant, in the range 10–15%. A normal stress, σ_1, between 25 and 257 kPa was imposed (see Table 1) by the way of lead dead weights. The macroscopic deformation of the samples was recorded through the experiment by measuring the vertical displacement using four LE12S-Solartron sensors, where one was used as a reference and the three others for the measurement (Fig. 2). The displacements were also recorded at a frequency of three measurements per hour.

3.3. Geometry and mineralogy analyses

Salt localisation within the porous network and its damaging effects were studied in the samples both in 3D and 2D using X-ray computed tomography (XRCT) on core samples and scanning electron microscopy (SEM) on polished thin sections, respectively.

3D geometry analysis was performed on several samples after an experiment using a home-built X-ray tomograph (Laboratory 3S-R, Grenoble). The method is based on the 3D reconstruction of X-ray attenuation properties of the different materials forming the rocks. As air, halite, calcite, silicates and oxides have significant different chemical compositions and density, their attenuation properties to X-rays vary. Therefore, they can be distinguished on the 3D images based on their grey level. The optical system used in the experiment provided a resolution of 36 µm. Data sets of $1500 \times 1500 \times 1900$ voxels

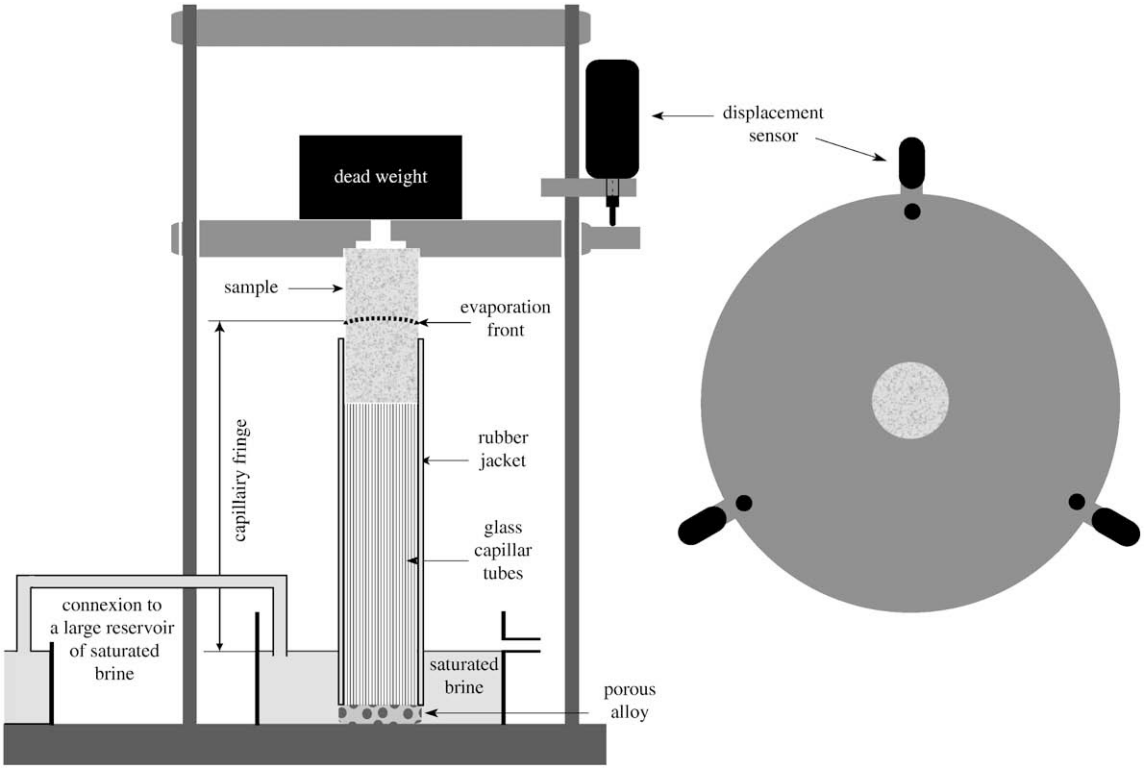

Fig. 2. Experimental set-up. a) The core sample is left in contact with glass capillary tubes such that the capillary height is controlled. The brine is located in a large reservoir, whose pressure head is controlled and remains constant. The load is imposed through lead dead weights; b) Top view of the apparatus: three displacement sensors measure the vertical displacement of the upper plate. By triangulation of these measurements, the vertical deformation of the core sample can be calculated.

Table 1
Experimental conditions and measured data.

Sample number	Rock	*T* (°C)	Stress (kPa)	Duration	Comments	Measurement deformation	Tomography	Thin sections
LAV-1	Limestone	30	0	48 days	Salt crystals around the sample	x		
LAV-2	Limestone	30	25	78 days	Salt crystals around the sample		x	x
LAV-3	Limestone	30	88	40 days	Salt crystals around the sample	x		
LAV-4	Limestone	30	132	78 days	Salt crystals around the sample	x	x	x
LAV-5	Limestone	30	171	40 days	Salt crystals around the sample	x		
LAV-6	Limestone	30	171	40 days	Salt crystals around the sample			
LAV-7	Limestone	30	257	78 days	Fracturing	x	x	x
LAV-8	Limestone	45	203	73 days	Salt crystals around the sample			x
LAV-9	Limestone	45	207	17 days	Fracturing		x	x
LAV-10	Limestone	45	207	73 days	Fracturing	x		x
ADA-1	Sandstone	45	221	73 days	Fracturing	x	x	x

were collected on five samples (see Table 1) and analysed using the Amira® 4.1 software.

Complementary to XRCT, SEM analyses were performed with a FEI Quanta-200 equipped with an energy dispersive X-ray detector (EDX). Observation of the sample morphology after experiment was made on frontal thin sections by detection of backscattered electrons (BSE). Secondary electron mode (SE) was also used to directly study the crystal morphology. EDX analysis was used to map the chemical composition of the different minerals forming the rocks and to localize the precipitation of salt.

4. Results

4.1. Macroscopic observations

The samples were removed from their holder after an experiment, and visual observations were performed. Two kinds of salt precipitation features can be observed. For some samples (LAV-1 to LAV-6, and LAV-8), the surface was covered with an efflorescence of salt above the upper limit of the rubber sleeve. When this salt crystallization crust was removed, the surface of the samples appeared as peeled (see LAV-8 and LAV-2 in Fig. 3. None of these samples showed any evidence of fracturing. For the other samples (LAV-7, LAV-9, LAV-10 and ADA-1), no crust of salt was visible at the sample surface above the sleeve, even if minor evidence of salt efflorescence could be seen. Conversely, all these samples were highly damaged by a set of fractures that has developed above the capillary fringe level (see Fig. 3, samples ADA-1, LAV-7 and LAV-9).

4.2. Deformation of the samples during salt precipitation

Evolution of the displacement with time is displayed for several samples in Fig. 4. A single curve is given for each sample, which represents the mean value of the three displacement sensors. All the samples showed a slight length decrease during the first days of the experiments, from 3 to 20 µm. The shrinkage, which is very small, may result from compaction induced by the weights that are loaded on the sample, especially along the surface of contact between the sample and the upper and lower plate of the experimental device.

Then two different behaviours, observed Fig. 4, can be associated to the two different halite crystallization patterns. Some samples kept the same length (LAV-1) or showed a very slight increase of length (of 10 µm for LAV-3 and LAV-5, and 20 µm for LAV-4). They correspond to samples for which well-developed salt efflorescences were observed. Conversely, a clear vertical extension was observed for samples for which fractures were observed. The increase of the sample length occurred after a period ranging from 10 (ADA-1) to 35 days (LAV-5), and may be related to the first fracturing stage of the sample. The displacements increased by steps, indicating that deformation was irregular in time. Vertical displacement could reach up to 100 µm (ADA-1).

4.3. 3D geometry of the precipitation patterns and fracture network

Imaging using X-ray tomography allows the 3D internal structure of the rocks to be displayed (Figs. 5 and 6). Fractured samples (LAV-7, LAV-9, LAV-10 and ADA-1) present a complex 3D fracture network. Despite the experiment duration for two of the three limestone samples

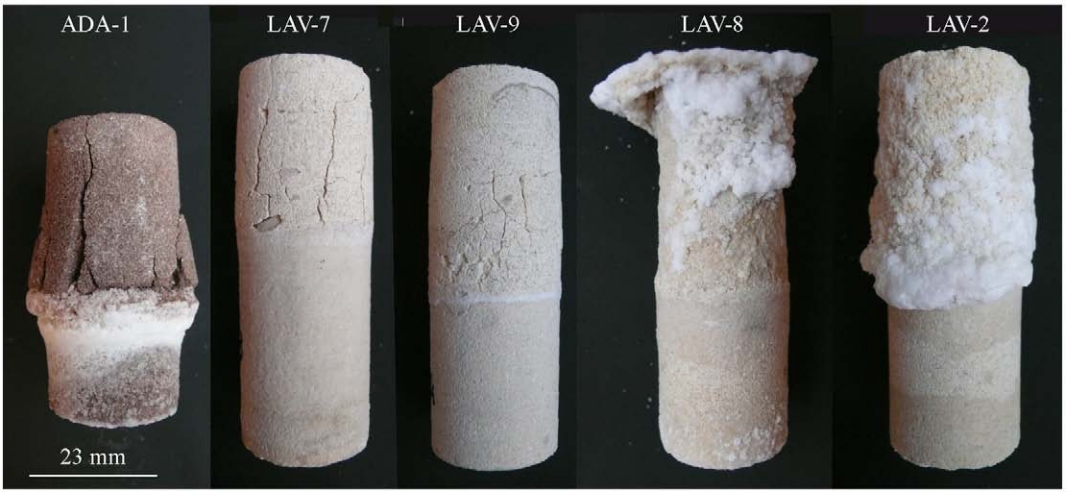

Fig. 3. Views of typical crystallization patterns on core samples after the experiments. The height of the capillary fringe varies between 100 and 150 mm and corresponds to the height where precipitation occurred either inside the sample (ADA-1, LAV-7 and LAV-9), leading to fracturing, or at the sample surface (LAV-8 and LAV-2) leading to the formation of a crust of salt. For each sample, the horizontal scale bar corresponds to 23 mm.

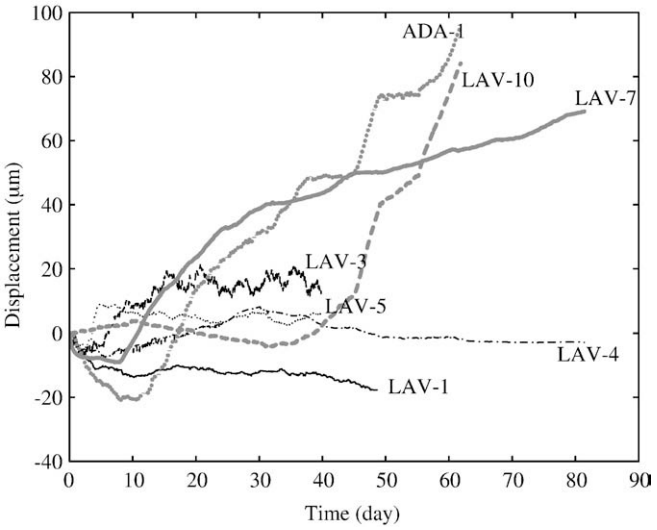

Fig. 4. Height of the sample as a function of time during salt capillary rise and precipitation. Samples that have intensively fractured (thick grey lines) show a vertical dilation up to 100 µm, whereas for samples that did not fracture (fine black lines), no significant deformation could be measured.

is comparable with the sandstone sample, the latter is more damaged and shows massive halite precipitation.

Two types of structures can be seen within these samples. Firstly, one or several parabolic bell-shaped overlapping fronts, whose diameter decreases from the bottom to the top of the samples, are highlighted by massive halite precipitation (Figs. 5b and 6b). In sandstone sample ADA-1 the number of parabolic fronts is very high (i.e. about eight), while it varies from two to four for the limestone samples. Halite precipitation patterns are related to the nature of the rock. For the limestone samples, halite appears to be "fibrous" in the main fractured front (Fig. 6b, d), with a preferred orientation of the fibres perpendicular to the evaporation surface. On the other hand, this pattern resembles a "cauliflower" for the sandstone sample (Fig. 5b, c). These fronts correspond to successive evaporation fronts where supersaturation of halite has been reached, inducing precipitation. Fractures wrapping these fronts can be observed.

Secondly, a set of radial fractures is observed. They take root on these parabolic fronts and reach the free surface (Figs. 5c, d and 6c, d). The radial fractures located at the base of the precipitation fronts are almost rooted perpendicularly to them and fracture planes are oriented vertically (as depicted in Fig. 6d). Conversely, fracture network at the upper part of the parabolic fronts is much more complex with main and secondary fractures. Most of these fractures do not show evidence of halite precipitation within them.

4.4. SEM observations

Both SEM images (Figs. 7 and 8) and elemental analysis (Fig. 9) do confirm the presence of halite and show crystals precipitated in localized places throughout the porous network. Precipitation of halite occurs mainly as blocky cubic (Fig. 8a) or large recrystallized (Fig. 8b) crystals. For limestone, there is rare evidence of precipitation in micro-porosity of micrite, and halite is mainly observed in the inter-grain porosity. For the non-fractured samples, halite precipitation occurred mainly at the sample surface, despite that some halite clusters can also be observed in some pores inside the sample (Fig. 8d). Intense halite precipitation associated with calcite grain peeling was observed in the efflorescences. The presence of several rounded crystals suggests partial redissolution of halite.

For the fractured samples, halite precipitation occurred mainly at the different parabolic evaporation fronts (Fig. 7). For both limestone and sandstone, intense fracturing can be associated to the precipitation of halite at the fronts, which often present a main fracture and a set of sub-collinear small fractures (Fig. 8e) partially or completely filled with halite. Floating grains or rock fragments can be observed in the areas of massive halite precipitation and fracturing. Individual grains of quartz, feldspar or calcite can be also affected by fracturing without distinction (Fig. 8e, f, g). For limestone samples LAV-7 and LAV-9, halite crystals have a specific morphology along the parabolic fronts. At the main halite precipitation front, where intense fracturing occurred, halite crystals present peculiar linear geometry (Fig. 8h). They appear as columnar crystals oriented perpendicularly to the evaporation front. Preferred halite crystal growth was not visible on the perfectly polished sections, but could be observed when a small amount of halite was dissolved at the surface of the thin section, and sub-grain boundaries could be revealed (Fig. 8i, j).

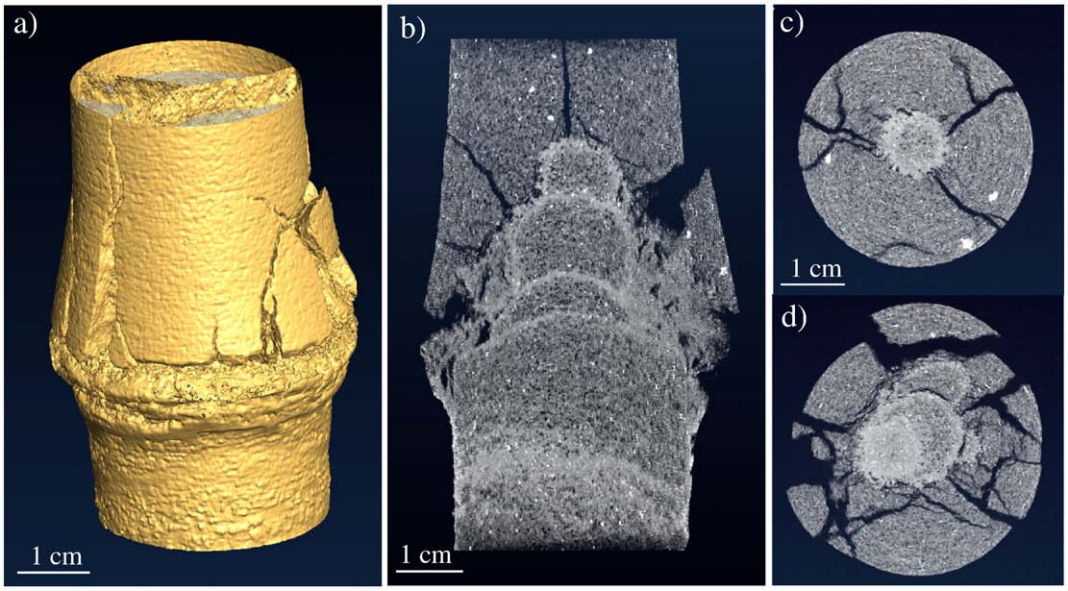

Fig. 5. X-ray tomography images of sample ADA-1; a) 3D view of the fractured sample; b) 2D frontal cross-section, and c) and d) 2D transverse cross-sections showing five different evaporation fronts where halite precipitation has occurred (light grey levels) and the radial fracture network (dark grey levels). Images c) and d) are obtained at around 1.3 and 3 cm from the top of the sample, respectively.

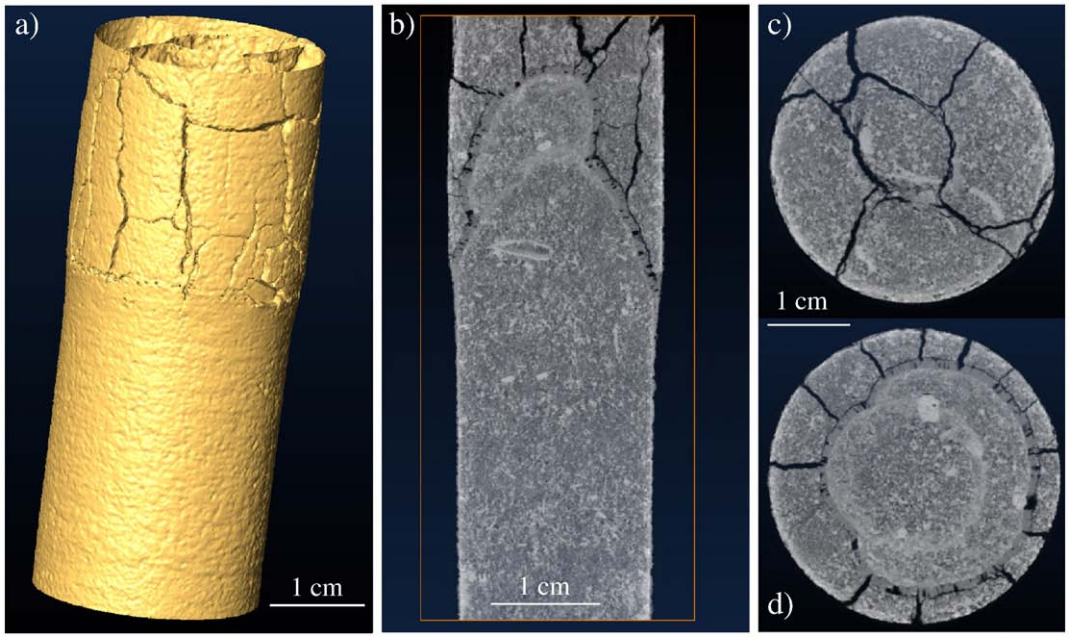

Fig. 6. X-ray tomography images of sample LAV-7; a) 3D view of the fractured sample; b) 2D frontal cross-section, and c) and d) 2D transverse cross-sections showing two imbricate evaporation fronts (light grey levels), and fibrous-like halite precipitates (intermediate grey level), and radial fracture network (dark grey levels). Images c) and d) are obtained at 0.4 and 1.8 cm from the top of the sample, respectively.

5. Discussion

5.1. Efflorescence versus fracturing

As seen in Figs. 3, 5 and 6, salt localization in the porous samples shows different patterns, with either fractured or non-fractured samples. While the capillary fringe is visible at a few centimetres under the upper surface of the fractured samples (ADA-1, LAV-7 and LAV-9), the capillary rise was higher than the sample height in non-fractured samples (LAV-8, LAV-1 to LAV-6). The reason is that, despite the different cores were drilled in the same block, the capillary rise was different between the samples, illustrating the variability of the pore throat distribution and porous network among the different samples.

When the capillary rise was higher than the sample height, evaporation occurred very close to the rock–air interface. As a consequence, halite crystals tend to grow from the pores located close to the sample surface, in direct contact with air. This produced the efflorescence pattern that contributed to damage the rock by salt crystallization. The damage was localized at the core periphery and the crystallization pressure was sufficient to tear rock particles from the surface. Then, the particles migrated embedded into halite crystals during salt growth, as observed with SEM (Fig. 8d).

Conversely, when the capillary rise was lower than the sample height, evaporation did occur in the interior of the rock sample. The parabolic shape of the evaporation front is directly related to the boundary conditions (see discussion below). When evaporation occurs, the saline solution becomes supersatured, causing halite precipitation and crystal growth along and near the evaporation surface. This process has two consequences. Firstly, intense fracturing of the rock-forming minerals is generally associated with the parabolic fronts. It leads to a distension of the sample above the parabolic crystallization front, which is responsible of the development of the radial fracture networks. Secondly, reduction of the pore sizes caused by halite precipitation increases the capillary height, leading to a slow upward propagation of the brine with time and the formation of the different overlapping parabolic fronts. This may explain that successive evaporation fronts formed (Figs. 5b and 6b). The temporal evolution of halite precipitation patterns is very complex, as precipitation causes a progressive sealing of the porous network, inducing a decrease of the evaporation rate at the front. Complete sealing of the evaporation front without the generation of associated fracture could finally block this dynamic system.

5.2. Estimation of the supersaturation

In the samples that broke, the force of crystallization was high enough to i) reach the tensile strength of the rock and fracture it, and ii) push vertically the dead load against gravity, therefore balancing at least the normal stress. Using a simple approach, one can tentatively estimate the range for the supersaturation assuming that the surface tension effect in the smallest pores is negligible. The saturation index Ω is related to the pressure through Eq. (8), where:

$$\Omega = \frac{a_{Na}a_{Cl}}{a_{0,Na}a_{0,Cl}} \approx \left(\frac{a_{Na}}{a_{0,Na}}\right)^2 = \exp\left(\frac{\Delta P V_s}{RT}\right). \quad (11)$$

Then, an estimation of the pressure difference ΔP can be proposed based on two different values. The minimum value corresponds to the pressure necessary to lift the dead weight; it is close to 0.2 MPa for most of the experiments. The other value corresponds to the tensile strength of the solid that was reached during the experiments and is in the range 1 to 10 MPa for limestones. Using $V_s = 2.7\ 10^{-5}\ m^3\ mol^{-1}$, $R = 8.32\ m^3\ Pa\ K^{-1}\ mol^{-1}$, $T = 303\ °K$, we obtain for ΔP in the range [0.2–10] MPa, a value Ω in the range [1.002–1.113] indicating a supersaturation between 2‰ to 11%, in the range of what has been calculated by Steiger (2005a). It is therefore clear that the last value is only indicative, considering that the local state of stress induced by halite crystal growth was approximated by the tensile strength, which is a macroscopic variable.

5.3. Fracturing mechanism

Despite the information provided by SEM and XRCT observations, it is difficult to establish a precise chronology of the different fracturing events. Furthermore, fracturing is irregular as indicated by the displacement curves (Fig. 4). Nevertheless, these observations

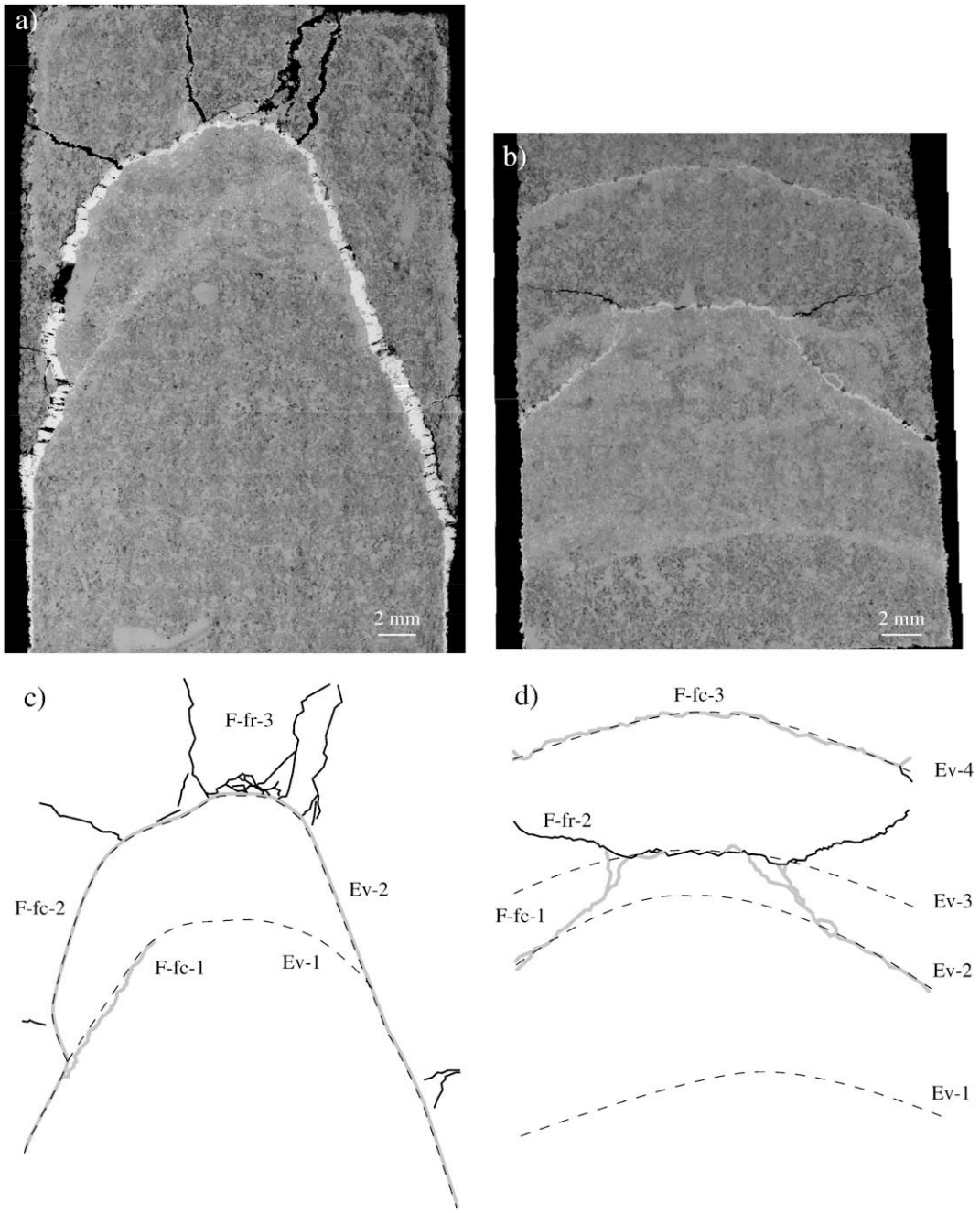

Fig. 7. Frontal cross-section through the samples LAV-7 (a) and LAV-10 (b) observed by SEM after experiment (each image corresponds to an assemblage of around 200 views) providing information on the chronology of fracturing mechanisms in relation with the different evaporation fronts (Ev-, black dotted line); c) and d) Sketch showing the fronts that are transformed into tensile cracks due to the force of crystallization (F-fc-, high grey line) and radial cracks due to accommodation (F-fr-, black line). The different numbers refer to the chronology of the events (evaporation or fracturing).

provide a better understanding of the relationship between halite precipitation and fracturing mechanisms, despite halite can also precipitate into cracks after fracturing (Fig. 8). Two main stages are involved in the fracturing mechanism: 1) formation of primary parabolic cracks at the evaporation front, 2) formation of secondary radial cracks upon it. At the evaporation fronts, the fracturing is more intense, and is induced when crystallization force exerted by halite precipitation is stronger than the tensile strength of the rock. A series of sub-collinear cracks can also be observed. Fracturing is initiated at the bottom of the evaporation front and propagates along it, where tensile stress is higher and favours the fracture propagation in mode I (i.e. opening mode, which implies that the two walls of the fracture move perpendicularly away from the fracture plane where the fracture forms). The main fracturing mechanism is fracture propagation running both through (intra-granular) and between (inter-granular) grains (Fig. 9). Individual grains intensively affected by fracturing are also noticed (Fig. 8g), and can result from local tensile or compressive stresses induced by either intra-granular or inter-granular crystallization pressure. Most of the time, the main primary crack develops and wraps entirely the parabolic curved evaporation front despite in some case it stops (Fig. 7a, c, F-fc-1) or links together two different evaporation fronts (Fig. 7b, d, F-fc-1-2). Once the primary cracks are formed, halite keeps growing inside. At some point, deformation of the sample is sufficient to involve the fracturing

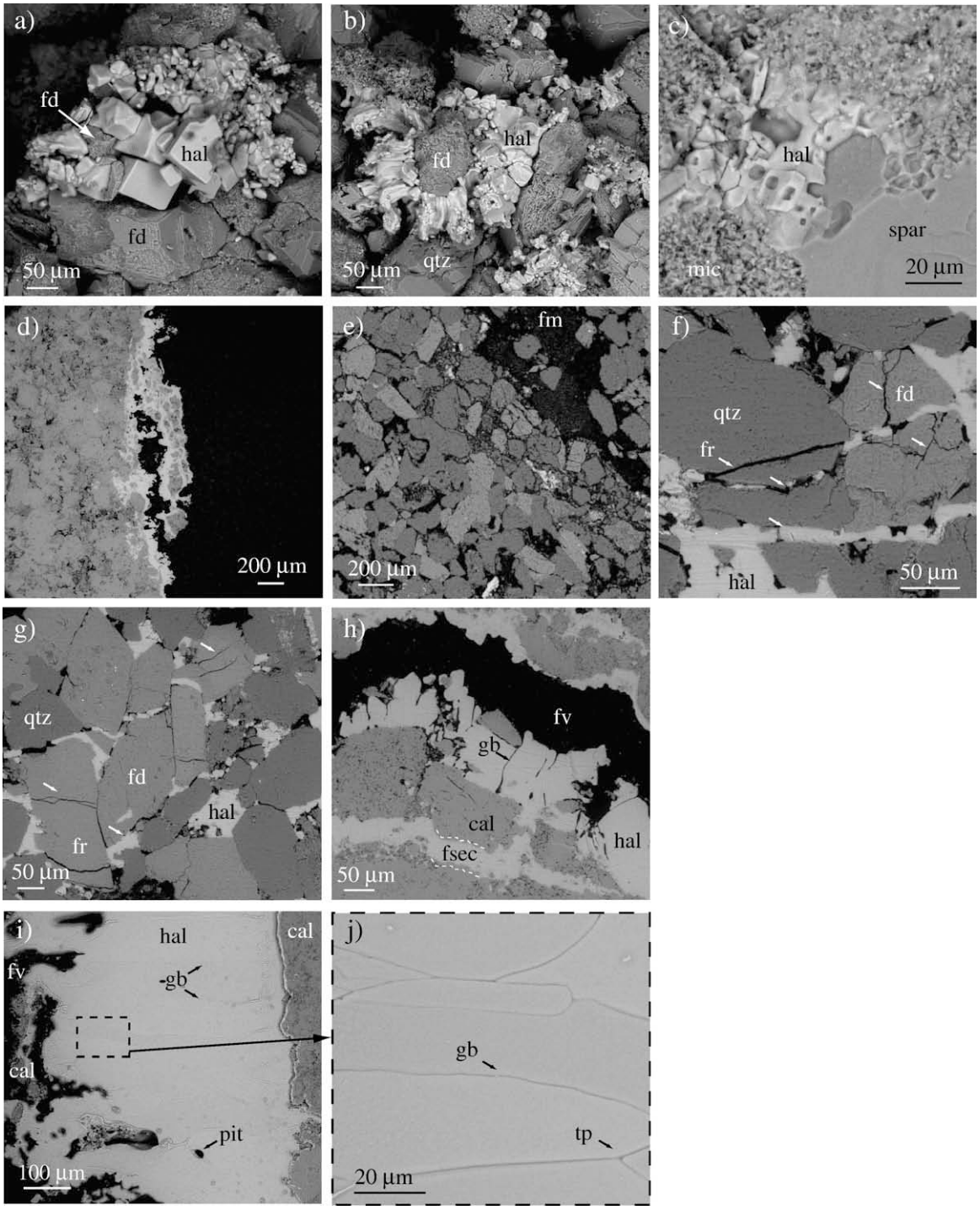

Fig. 8. SEM-BSE observations a) blocky cubic crystals of halite associated to cracking of a feldspar (ADA-1); b) large blocky crystals of halite precipitated around a feldspar (ADA-1); c) blocky crystal of halite in (LAV-7); it is worth noting that halite did not precipitate in the micrite intra-porosity. In this case, small pore diameters may prevent crystallization as explained in Fig. 1b; d) peeling process (LAV-4): salt crystals (light grey levels) have precipitated in the pores near the sample surface, leading to the detachment of calcite particles (intermediate grey levels); e) fracture network close to one of the parabolic crystallization front (ADA-1): cracked grains of quartz and feldspar are clearly visible in the multi-fractured damage area. Note that halite has been partially redissolved in this area to allow a better visualisation of the fracture network; f) and g) details of cracked feldspar and quartz grains (ADA-1): halite partially filled some cracks and grain joints; h) fracture void at the top of the parabolic crystallization front (LAV-9), showing the distribution of halite crystals around the calcite grains. Clean fracturing of the sparite crystals is visible in the secondary sub-collinear fracture (dotted lines). While lower secondary fracture is completely sealed with halite, partial redissolution of halite in the main fracture evidences sub-grain boundaries mainly oriented perpendicularly to the fracture; i) fracture void at the bottom of the parabolic crystallization front (LAV-7) and j) details of sub-grain boundaries preferentially oriented in the direction of crystallization. Sub-grains were evidenced after slight redissolution of halite. Legend: hal: halite; qtz: quartz; fd: feldspar; mic: micrite (calcite); spar: sparite (calcite); fr: fracture, fm: main fracture, fsec: secondary fracture; fv: fracture void; gb: grain boundary; cal: calcite tp: triple junction.

of secondary cracks, which develop to accommodate the deformation and to compensate for the sample volume increase. Most of these secondary cracks are rooted perpendicularly to the evaporation front (Figs. 5b, c, 6b, d, and 7a, b), despite that the network is much more complex and involves the formation of sub-cracks (Figs. 5d and 6c). As also seen in Figs. 5 and 6, crack opening measured vertically

appears larger than the vertical displacement recorded by the sensors (Fig. 4). Sample fracturing occurs above the crystallization fronts, with possible block displacement along the cracks that have been induced by the crystallization. This could be equivalent to the effects of normal faults (vertical shortening and horizontal elongation) and may accommodate part of the vertical displacement induced by the crystallization. Consequently, there is a competition between the uplift induced by halite growth and the sinking involved by fracture displacement. Fig. 10 highlights the different mechanisms involved in the fracturing process.

The experiment brings a new look on the mechanisms according to which fractures developed and are sealed in nature since here mineral crystallization is the driving force for fracture opening along the evaporation front, contrary to common assumption that fractures open first then are sealed. Another important feature is that crystallization acts as a forcing parameter to promote secondary non-sealed fracture network. For an application to the storage of saturated fluid that could evaporate in geological reservoir, the question is then to know how permeability may evolve with time in such a process. In our experiments, the progressive decrease of the size of the successive sealing fronts indicates a progressive decrease of the permeability with time despite the development of a secondary fracture network. This happens because the secondary network develops in the forefront of the migrating sealing front. However, in natural deformation the formation of such intense fracture networks may at least locally increase the permeability of the reservoir.

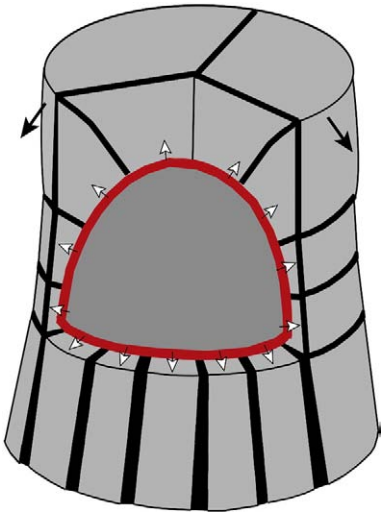

Fig. 10. Interpretative sketch of the parabolic evaporation interface that produce local overpressure (white arrows) and fracturing processes that induce secondary sets of radial fracture networks (black) perpendicular to the fracturing-sealing front. Black arrows indicate displacement of fractured blocks.

5.4. Model of evaporation and transport in the solid

The shape of the evaporation front depends strongly on the evaporation boundary conditions and the domain limits (i.e. the sample shape and size). Considering core sample for which evaporation is allowed at the top and around, fluid rising results in the formation of a bell-shaped parabolic evaporation front. In this section, we propose a simple analytical model to calculate the shape of the parabolic evaporation fronts observed in fractured samples (LAV-7, LAV-9, LAV-10, and ADA-1). Let us consider a porous medium where a fluid is rising due to a balance between capillary forces and gravity. The fluid is evaporating within the porous solid. The evaporation front represents an equilibrium interface between fluid rising and evaporation, where salt precipitation occurs. The problem is supposed

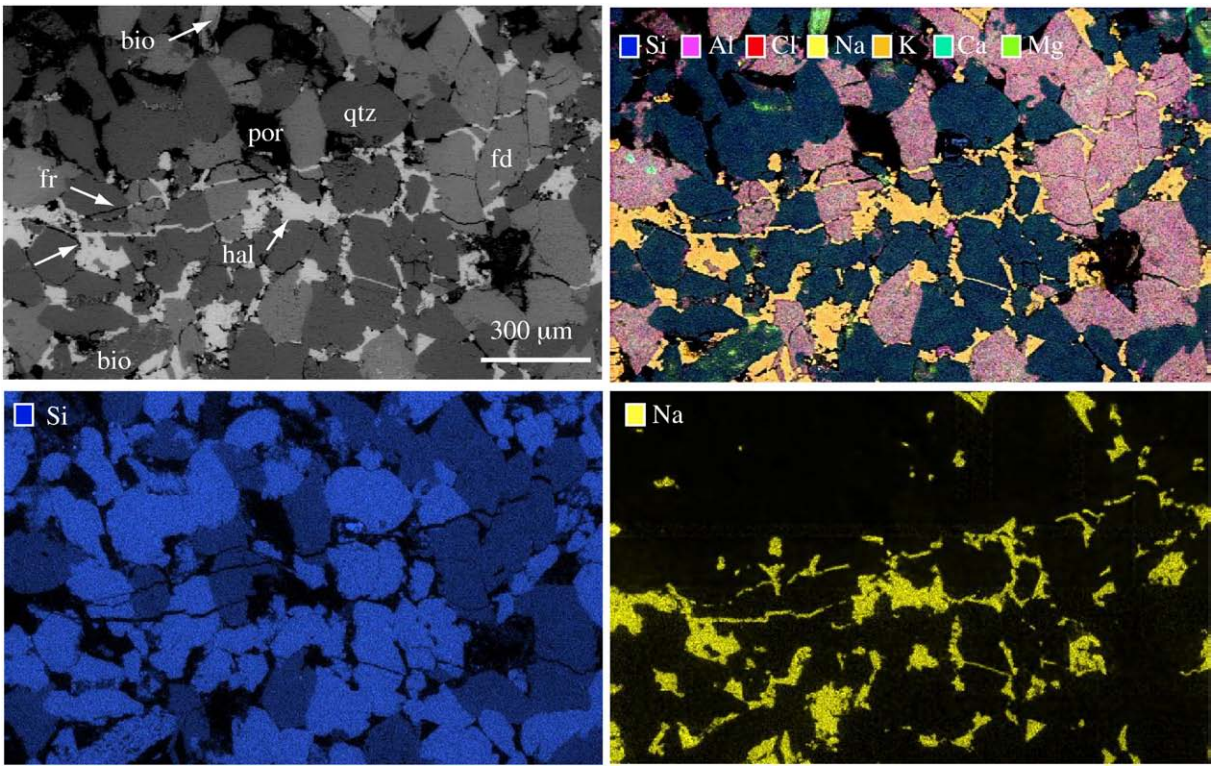

Fig. 9. SEM-EDX chemical mapping of the cracked region of the sample ADA-1, showing the distribution of halite. Fractures propagated mainly along grain boundaries, but also several intra-granular cracks are visible.

axisymmetric around the cylindrical sample, so that unknowns are only dependent on the radial distance r to the cylinder axis. Four unknown variables are needed to describe the physics of this problem: μ (m s^{-1}), the vertical velocity of the rising fluid, h (m), the height of the water column in the porous medium (i.e. the position of the evaporation front), j (kg m^{-2} s^{-1}), the evaporation flux at the evaporation front, and P (Pa), the fluid pressure.

Firstly, we consider the conservation of momentum on a vertical column that contains liquid and vapour and that is located at a distance r_0 from the centre of the sample (see Eq. (1) in Ramona and Oron, 2008):

$$\rho\frac{d(hu)}{dt} = \frac{2\sigma\cos(\theta)}{R} - \rho g h - \frac{8\mu}{R^2}hu \tag{12}$$

where ρ (kg .m^{-3}) is the density of the liquid, g (m .s^{-2}) is the constant of gravity, μ is the dynamic viscosity of the liquid (N m^{-2} .s), R is the radius of the capillary tube, σ (N .m^{-1}) is the interfacial tension, and θ is the wetting angle. In Eq. (7), the first term on the right hand side represents the capillary force that drives the fluid, the second term represents the gravity force, and the third term stands for the viscous drag.

Secondly, we consider mass conservation along a vertical fluid–vapour column:

$$\rho\left(u - \frac{dh}{dt}\right) = j \tag{13}$$

where j (kg .m^{-2} .s^{-1}) represents the evaporation mass flux along the liquid–vapour interface, this interface being located inside the porous sample or at its surface.

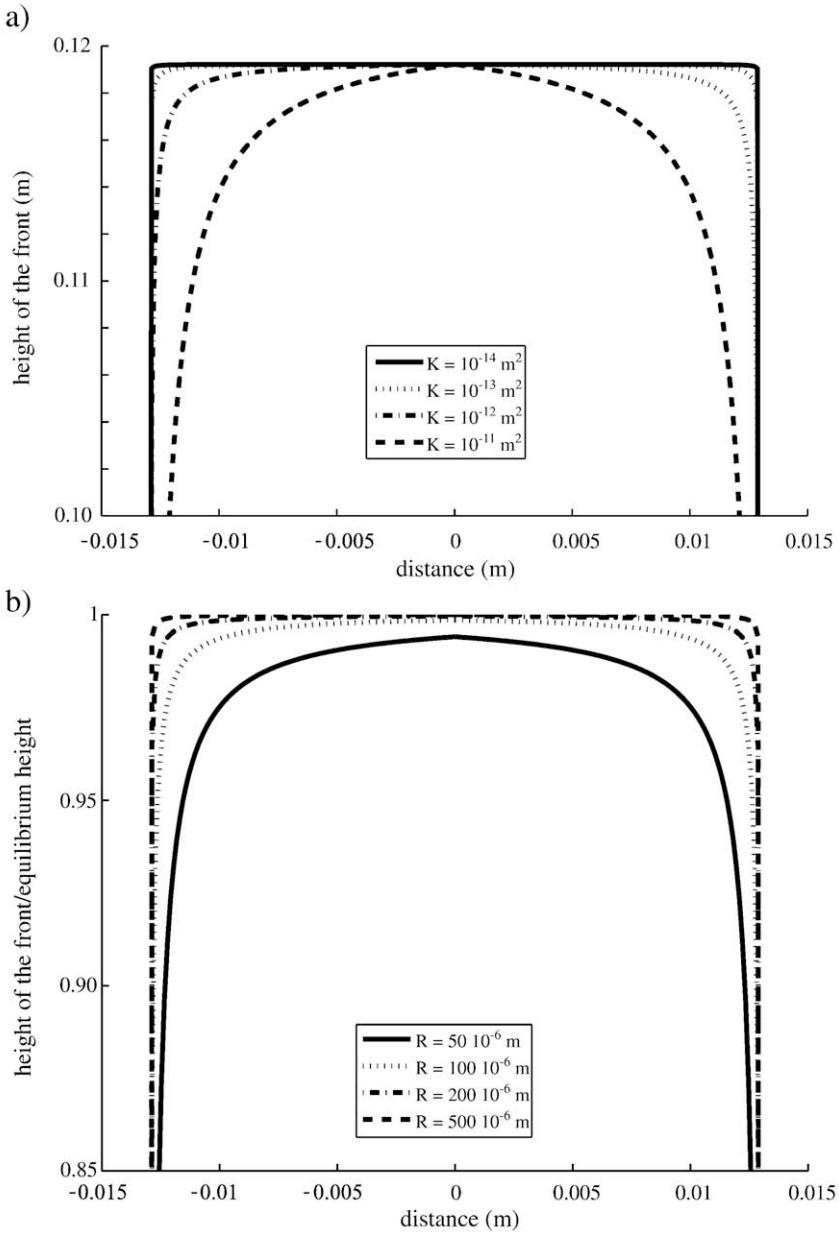

Fig. 11. Simulation of the position of the evaporation front in the porous sample using Eq. (13) showing the effects of permeability and pore radius. a) The radius of the pores is fixed at $R = 100$ μm and the permeability is varied between 10^{-14} and 10^{-11} m^2. b) Similar simulations with $k = 10^{-12}$ m^2 and pore radius in the range 50–500 μm. Here, the height of the front is normalized to the equilibrium height of a capillary fringe.

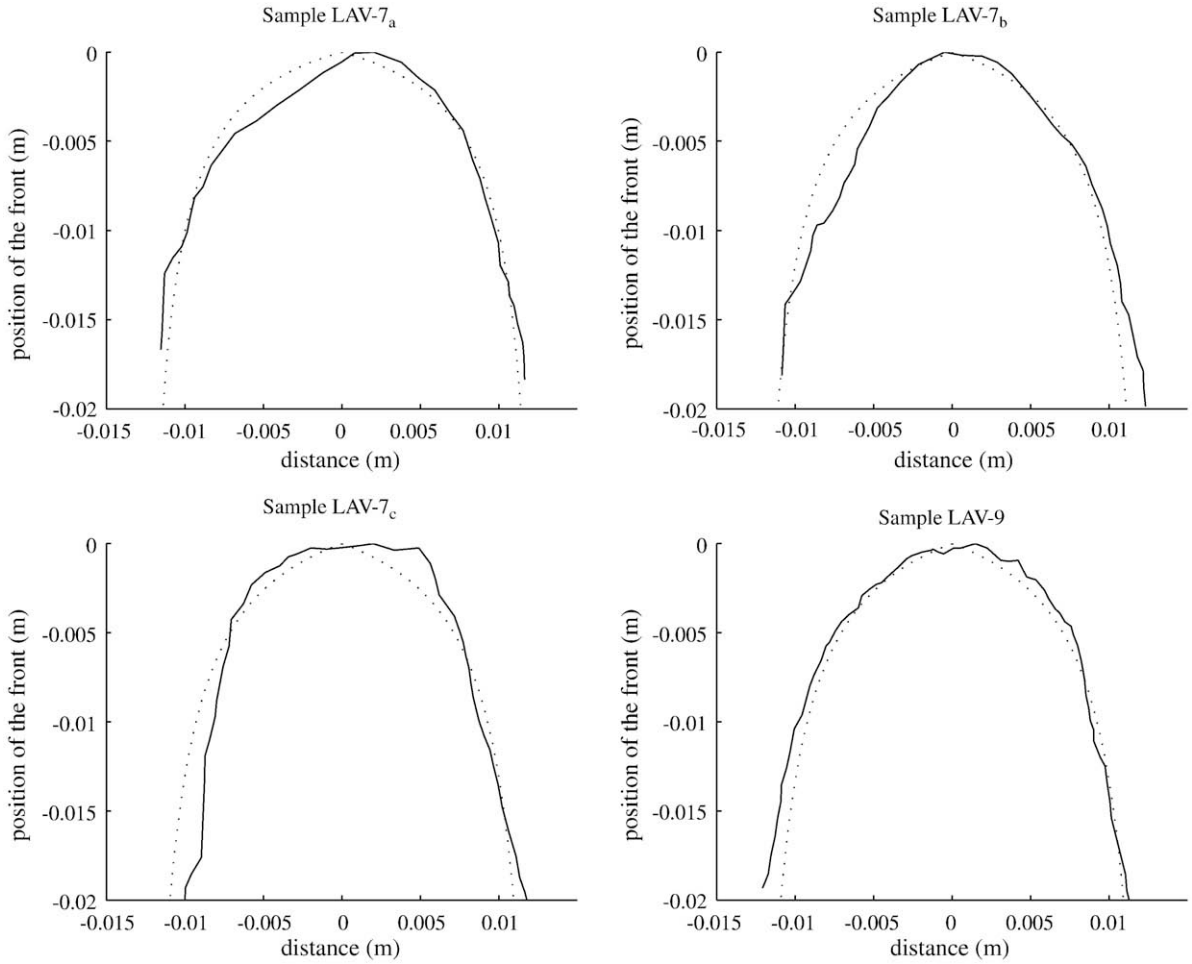

Fig. 12. Position of the evaporation fronts in samples LAV-7 and LAV-9 (black lines) and best fits (dotted lines). For samples LAV7, the three curves correspond to three successive positions of the evaporation front. The fits are done using the model of Eq. (11). Interface LAV7$_a$: $R=80$ μm, $k=10^{-11}$ m^2; interface LAV7$_b$: $R=70$ μm, $k=0.8\cdot10^{-11}$ m^2; interface LAV7$_c$: $R=65$ μm, $k=0.7\cdot10^{-11}$ m^2; interface LAV9: $R=70$ μm, $k=0.9\cdot10^{-11}$ m^2.

Then, we consider the transport of vapour in the porous medium, from the evaporation interface to the air oven. We assume that the vapour diffusion is purely radial so that the diffusion law becomes:

$$\frac{1}{r}\frac{\partial}{\partial r}\left(r\frac{\partial P}{\partial r}\right)=D\frac{\partial P}{\partial t} \tag{14}$$

where D (m^2.s^{-1}) is a diffusivity constant. This partial differential equation requires two boundary conditions. At the boundary of the sample of radius $r=a$, P is equal to P_w, the partial pressure of water in the air oven. At the liquid–vapour interface $r=r_0$, the pressure $P(r,h(r))$ is equal to P_s, the saturation pressure of water at which evaporation occurs. The latter relationship gives the equation for the interface $h(r)$. To summarize:

$$\begin{matrix} P(r=a)=P_w \\ P(r=r_0)=P_s \end{matrix}. \tag{15}$$

Finally, the evaporation flux can be calculated assuming Darcy flow of the vapour into the porous medium. Assuming a permanent regime:

$$j=-\frac{k}{\mu_V}\rho_V\frac{\partial P}{\partial r}\Big|_{r=r_0}=-\frac{k}{\mu_V}\rho_V\frac{P_w-P_s}{a-r_0} \tag{16}$$

where k (m^2) is the permeability of the porous medium, and μ_V (Pa s) and ρ_V (kg m^{-3}) are the dynamic viscosity and density of the water vapour, respectively.

For a permanent regime, Eq. (13) becomes:

$$u=\frac{k}{\mu_V}\frac{\rho_v}{\rho}\frac{P_s-P_w}{a-r_0} \tag{17}$$

and using (Eq. 12) yields:

$$h=\frac{\frac{2\sigma\cos(\theta)}{R}}{\rho g+\frac{8\mu_V}{R^2}\frac{k}{\mu_V}\frac{\rho_v}{\rho}\frac{P_s-P_w}{a-r_0}}, \tag{18}$$

which represents the equilibrium position of the fluid–vapour front inside the porous medium, as a function of the transport properties of the solid and the nature of the fluid.

5.5. Localization of the evaporation front into the porous medium

The position of the salt precipitation front in the experiments can be calculated using Eq. (18), with parameters that are relevant for the two rock samples: $\mu_V=2\cdot10^{-5}$ Pa s, $\rho_V=1.2$ kg m^{-3}, $\rho=1190$ kg m^{-3}, $g=9.82$ m s^{-2}, $\sigma=0.072$ N m^{-1}, $\theta=0°$, $P_s=7.35$ kPa at 40 °C, $P_w=0.2\cdot P_s$, $a=0.012$ m. Two petrophysical parameters of the rock can be

varied, i.e. the radius of the pores R in the range $50–500 \cdot 10^{-6}$ m, and the permeability k in the range 10^{-14}–10^{-11} m^2. The results are shown in Fig. 11. These two parameters control the shape of the evaporation interface, and the permeability has a strong effect. Indeed, for higher permeability, the vapour transport flux is higher from the porous medium to the free air and allows the localization of the precipitation inside the porous medium.

Finally, to verify the model, the position of the evaporation fronts in samples LAV-7 and LAV-9 was extracted from XRCT images. To fit the shape of these fronts, it is possible to apply Eq. (18) using parameters relevant for the type of rock used in the experiments (Fig. 12). Moreover, this model also shows that if either the pore radius or the permeability decreases, the evaporation front should be displaced in the upper direction and become also narrower. This is what is observed for samples LAV-7 and ADA-1, where successive precipitation fronts have formed. These fronts can be interpreted as resulting from salt precipitation coupled to both pore radius and permeability reduction. It is shown in Fig. 12 (bottom) that it is possible to fit the shape of the successive fronts using decreasing values for the permeability and the pore radius.

6. Conclusion

The relation between halite precipitation and fracturing mechanisms was investigated in a salty water drying experiment where we used cylindrical cores of porous rocks loaded by dead weights ($25 < \sigma_1 < 257$ KPa). These experiments provide new information on the sealing and fracturing mechanisms associated to mineral precipitation within rocks. Results of this experiment identify the control exerted by halite precipitation on the fracturing of porous rock. Two different behaviours were observed within the rock samples. When the capillary fringe is higher than the sample height, evaporation occurs only around the sample, involving peeling process and particle displacement related to halite crystal growth. Conversely, when the capillary fringe is located within the interior of the sample halite precipitation occurs along one or several parabolic evaporation fronts and induce intensive fracturing of the rocks in the forefront of the sealing parabolic surfaces and displacement of grains.

Two different mechanisms were involved in the fracturing process. The first mechanism is individual grain crushing and both intra- and inter-granular crack propagation resulting directly from halite precipitation at the evaporation front. Fracturing occurs when the crystallization pressure is higher than the tensile strength of the rock and cracks propagate by wrapping the parabolic curved evaporation front, where tensile stress induced by halite crystal growth is larger. The second mechanism is a fracturing process as an accommodation of the deformation involved in the sample by the first fracture-sealing mechanism.

Finally, a capillary rise model has been developed to explain the shape of the evaporation front. The model explains the position of the front in the sample, depending on external thermodynamic parameters.

Acknowledgments

This work was supported by the Agence Nationale de la Recherche (ANR-05-CO2-009-04 "Geocarbon Carbonation project" and ANR-09-JCJC-0011-01 grants) and by Gaz de France. We would like to thank Jacques Desrues from the 3S-R laboratories for his help with the X-ray microtomograph, Robert Guiguet for building the deformation rig, Sylvie Regnier for thin section preparation and Philippe Recourt for SEM assistance and image assemblage.

References

Angeli, M., Benavente, D., Bigas, J.-P., Menéndez, B., Hébert, R., David, C., 2008. Modification of the porous network by salt crystallization in experimentally weathered sedimentary stones. Materials and Structures 41, 1091–1108.
Chatterjee, A., Raymahashay, B.C., 1998. Spheroidal weathering of Deccan Basalt: a three-mineral model. Quarterly Journal of Engineering Geology 31, 175–179.
Chatterji, S., 2000. A discussion of the paper Crystallisation in pores by G.W. Scherer. Cement and Concrete Research 30, 669–671.
Correns, C.W., 1949. Growth and dissolution of crystals under linear pressure. Discussions of the Faraday Society 5, 267–271.
Correns, C.W., Steinborn, W., 1939. Experiments for measuring and explaining the so-called crystallization strength. Zeitschrift Fur Kristallographie 101 (1/2), 117–133.
David, C., Wong, T.-F., Zhu, W., Zhang, J., 1994. Laboratory measurements of compaction-induced permeability change in porous rocks: implications for the generation and maintenance of pore pressure excess in the crust. Pure and Applied Geophysics 143, 425–456.
Dysthe, D.K., Renard, F., Porcheron, F., Rousseau, B., 2002. Water in mineral interfaces — molecular simulations of structure and diffusion. Geophysical Research Letters 29, 13208–13211.
Everett, D.H., 1961. The thermodynamics of frost damage to porous solid. Transactions of the Faraday Society 57, 1541–1551.
Flatt, R.J., 2002. Salt damage in porous materials: how high supersaturations are generated. Journal of Crystal Growth 242, 435–454.
Flatt, R.J., Steiger, M., Scherer, G.W., 2007. A commented translation of the paper by C.W. Correns and W. Steinborn on crystallization pressure. Environmental Geology 52 (2), 221–237.
Fletcher, R.C., Merino, E., 2001. Mineral growth in rocks: kinetic–rheological models of replacement, vein formation, and syntectonic crystallization. Geochimica et Cosmochimica Acta 65, 3733–3748.
Lavalle, J., 1853. Recherche sur la formation des cristaux à la température ordinaire. Comptes Rendus de l'Académie des Sciences 36, 493–495.
Maliva, R.G., Siever, R., 1988. Diagenetic replacement controlled by force of crystallization. Geology 16, 688–691.
Muller, N., Qi, R., Mackie, E., Pruess, K., Blunt, M.J., 2009. CO_2 injection impairment due to halite precipitation. Energy procedia 1 (1), 3507–3514. doi:10.1016/j.egypro.2009.02.143.
Owen, B.B., Brinkley, S.R., 1941. Calculation of the effect of pressure upon ionic equilibrium in pure water and in salt solutions. Chemical Society Reviews 29, 461–474.
Putnis, A., 2002. Mineral replacement reactions: from macroscopic observations to microscopic mechanisms. Mineralogical Magazine 66, 689–708.
Ramona, G., Oron, A., 2008. Capillary rise of a meniscus with phase change. Journal of Colloid and Interface Science 327 (1), 145–151.
Renard, F., Ortoleva, P., 1997. Water films at grain–grain contacts: Debye–Hückel, osmotic model of stress, salinity and mineralogy dependence. Geochimica et Cosmochimica Acta 61, 1963–1970.
Rijniers, L.A., Huinink, H.P., et al., 2005. Experimental evidence of crystallization pressure inside porous media. Physical Review Letters 94.
Rodriguez-Navarro, C., Doehne, E., 1999. Salt weathering: influence of evaporation rate, supersaturation and crystallization pattern. Earth Surface Processes and Landforms 24, 191–209.
Royne, A., Jamtveit, B., Mathiesen, J., Malthe-Sorenssen, A., 2008. Controls on rock weathering rates by reaction-induced hierarchical fracturing. Earth and Planetary Science Letters 275 (3–4), 364–369.
Ruiz-Agudo, E., Mees, F., Jacobs, P., Rodriguez-Navarro, C., 2007. The role of saline solution properties on porous limestone salt weathering by magnesium and sodium sulfates. Environmental Geology 52, 269–281. doi:10.1007/s00254-006-0476-x.
Scherer, G.W., 2004. Stress from crystallization of salt. Cement and Concrete Research 34, 1613–1624.
Scherer, G.W., 2006. Internal Stress and Cracking in Stone and Masonry. *6th European Conf. Fracture*, Alexandropoulis, Greece.
Steiger, M., 2005a. Crystal growth in porous materials I: the crystallization pressure of large crystals. Journal of Crystal Growth 282, 455–469.
Steiger, M., 2005b. Crystal growth in porous materials II: influence of crystal size on the crystallization pressure. Journal of Crystal Growth 282, 470–481.
Steiger, M., Linnow, K., Juling, H., Brüggerhof, S., Kirchner, D., 2008. Hydration of $MgSO_4 \cdot H_2O$ and generation of stress in porous materials. Crystal Growth and Design 8, 336–343.
Taber, S., 1916. The growth of crystals under external pressure. American Journal of Science 41, 532–556.
Wellman, H.W., Wilson, A.T., 1965. Salt weathering, a neglected geological erosive agent in coastal and arid environments. Nature 205, 1097–1098.
Weyl, P.K., 1959. Pressure solution and the force of crystallization — a phenomenological theory. Journal of Geophysical Research 64, 2001–2005.
Wiltschko, D.V., Morse, J.W., 2001. Crystallization pressure versus crack seal as the mechanism for banded veins. Geology 29, 79–82.
Winkler, E., Singer, P., 1972. Crystallization pressure of salts in stone and concrete. Geological Society of America Bulletin 83, 3509–3514.
Zehnder, K., Arnold, A., 1989. Crystal growth in salt efflorescence. Journal of Crystal Growth 97, 513–521.